where: $i \in [1..N]$, $\otimes$ represents the NCC operator, $*$ is the convolution operator, $T_{i,s}$ represents a test patch indexed by $i$, and $N$ is the number of test patches.

The test patches $T_{i,s}$ and the filter patch $P_s$ are from the same image ensemble. In our simulations, described in Section 5, we used $N = 2000$ test patches.

### 3.2. Resolution Similarity Function

To compare the responses of a patch for different resolutions, we define the Resolution Similarity Function (RSF), that is obtained by computing the normalized cross-correlations between the Patch Response Vector of the patch at the highest resolution $s_0 = 41$, and the Patch Response Vector of the patch obtained at some lower resolution $s$. The RSF is given by equation (2):

$$RSF(\mathbf{V}_{s_0}, \mathbf{V}_s) = \mathbf{V}_{s_0} \otimes \mathbf{V}_s \tag{2}$$

In Section 4 we provide a theoretical analysis of the RSF and in Section 5, we show quantitative simulation results for the different image ensembles.

## 4. Analysis of the Resolution Similarity Function

In this section, we provide a theoretical analysis of the RSF as a function of the resolution $s$.

We start by expressing the entries of the Patch Response Vectors as a function of the patch Fourier components and the Fourier components of the blurring Kernel $G_s$. We also assume the patches, in pixel space, are normalized to mean 0 and standard deviation 1, which is done a-priori in NCC matching:

$$V_{i,s} = P_s \otimes T_{i,s} = K \sum_j P_s^j . \overline{T_{i,s}^j} \tag{3}$$

$$= K \sum_j P_{s_0}^j . \overline{T_{i,s_0}^j} . |G_s^j|^2 \tag{4}$$

$$V_{i,s_0} = K \sum_j P_{s_0}^j . \overline{T_{i,s_0}^j} \tag{5}$$

Here, $K$ is a normalizing constant, $P_s^j$ and $T_{i,s}^j$ represent the complex Fourier component $j$ or the filter patch $P_s$ and the test path $T_{i,s}$ respectively, at resolution $s$. The sums are over all the complex Fourier components $j$. $\overline{x}$ is the conjugate operator. $|x|$ represents the norm. Eq. (4) results from the definition in eq. (1). We can ignore the down-sampling.

We can now express the RSF:

$$RSF(\mathbf{V}_{s_0}, \mathbf{V}_s) = \mathbf{V}_{s_0} \otimes \mathbf{V}_s \tag{6}$$

$$= \frac{\sum_i V_{i,s} . V_{i,s_0}}{\sqrt{\sum_i {V_{i,s}}^2 . \sum_i {V_{i,s_0}}^2}} \tag{7}$$

where the index $i$ goes over all the test patches.

In eq. (7), we assumed that the mean of $V_{i,s}$ and $V_{i,s_0}$ is 0. This is justified when the number of test patches is sufficiently large so that $V_{i,s}$ and $V_{i,s_0}$ cover uniformly the whole spectrum of responses, from -1 to 1.

We now consider the upper term of eq. (7) and replace $V_{i,s}$ and $V_{i,s_0}$ by their definition in eqs. (4) and (5):

$$\sum_i V_{i,s} . V_{i,s_0} = \tag{8}$$

$$\sum_i \sum_j P_{s_0}^j . \overline{T_{i,s_0}^j} . |G_s^j|^2 . \overline{\sum_j P_{s_0}^j . \overline{T_{i,s_0}^j}} \tag{9}$$

$$= \sum_{i,j} |P_{s_0}^j|^2 . |T_{i,s_0}^j|^2 . |G_s^j|^2 \tag{10}$$

In eq. (9), we used the fact that $V_{i,s_0} = \overline{V_{i,s_0}}$, since $V_{i,s_0}$ is a real number. In eq. (10), the fourth order terms representing the correlations between the components of different frequencies, that should appear, actually cancel out by assuming the different frequency components are not correlated over the image ensemble. This is not necessarily true, but we found that they are dominated by the terms present in eq. (10) (data not shown here). This assumption is also justified by the very good fit between the experimental curves and theoretical predictions shown in Section 5.

Finally, we assume that individual patches of the same ensemble have a Fourier amplitude spectrum close to the average amplitude spectrum over the ensemble, that we denote $\mathbf{Q}_{s_0}$ [13, 19]. This is an approximation for natural and car image patches, while it is exact for the $f^{-0.5}$ noise images. The final expression for $\sum_i V_{i,s} . V_{i,s_0}$ becomes:

$$\sum_i V_{i,s} . V_{i,s_0} = \sum_j {Q_{s_0}^j}^4 . |G_s^j|^2 \tag{11}$$

We can apply similar considerations for both sums in the denominator of eq. (7), and obtain the final expression of the RSF:

$$RSF(\mathbf{V}_{s_0}, \mathbf{V}_s) = \frac{\sum_j {Q_{s_0}^j}^4 . |G_s^j|^2}{\sqrt{\sum_j {Q_{s_0}^j}^4 . \sum_j {Q_{s_0}^j}^4 . |G_s^j|^4}} \tag{12}$$

Equation (12) entirely describes the behavior of the RSF as a function of the resolution (size), through the resolution dependent blurring Kernel $G_s$, and the average Fourier amplitude spectrum of the image ensemble, represented by $\mathbf{Q}_{s_0}$.

## 5. Experimental results

In this section, we present the simulation results. We show the RSF curves as a function of resolution (size) obtained experimentally for the different image ensembles, together with the RSF predicted by equation (12).

The results are summarized in Figure 3. The curves in the figure were obtained as follows. For a given image ensemble, 200 filter patches were selected randomly. For each filter patch, 2000 test patches were randomly chosen from the same ensemble. The RSF curve was then obtained according to equations (1) and( 2). The curves shown in the figure are the average curves over the 200 RSF curves obtained for the individual filter patches. To plot the theoretical predictions, we computed $Q_{s_0}$ by averaging the norm of the 2000 test patches Fourier amplitudes. We then plugged $Q_{s_0}$ and the spectrum of the filtering Kernel $\mathbf{G}_s$ into equation (12). 1-D cuts of the amplitude spectra $Q_{s_0}$, for the different image ensembles, are shown in Figure 4, illustrating in particular the stronger components at high frequencies in the noise images.

In Figure 3, we observe the graphs from right to left, and see that the curves for natural and car image ensembles remain very close to 1, up to the lower resolutions of $s = 15$ and $s = 10$ respectively, when the curves cross the RSF value of 0.99. Beyond these resolutions, the curves appear to drop more significantly. This indicates that the response properties of the patches are not affected by loss of visual detail until these lower limits. As shown in our theoretical analysis, the variations of the RSF, and thereby the values of the limit resolutions, are directly related to the form of the image ensemble amplitude spectrum, that is roughly of the form $f^{-1}$ for both cars and natural scenes [13, 19]. In contrast, the RSF of the $f^{-0.5}$ noise images falls off sharply at the onset of resolution reduction, because the low frequency components are less dominant. The RSF value is 1 for $s = 41$, since this is the original resolution of the patches.

While the RSF curves of individual filter patches do not have to be equal to one another, the deviations of the RSF values are necessarily very small up to the limit resolutions because the curves hold tightly to the maximum value of 1. Therefore, we omitted indications of variance for clarity.

We illustrate the resolution limits by also showing examples of filter-patches at different resolutions, with their individual RSF values, in Figures 5, 6 and 7. The different figures correspond to the three different image ensembles tested. Plotting the values displayed in these figures in the $(RSF(s), s)$ plane would yield an individual RSF curve. For example, from left to right, top to bottom in Figure 5, the RSF value of the natural filter-patch remains 1 (up to a precision of 0.01) until a resolution of $s = 15$, then it begins to drop. For the car filter-patch, the limit observed in Figure 6 is $s = 11$. For the $f^{-0.5}$ noise image patch, the decrease in the RSF value is immediate.

## 6. Discussion and conclusion

In the present study, we measured the responses of filter-patches to a large set of test-patches, extracted from within a same image ensemble, using Normalized Cross-Correlation as the matching measure. By comparing the set of responses obtained for high and reduced image patch resolutions, we showed, in simulations and by a simple theoretical calculation, how the set of patch responses depends on the image ensemble spectral statistics. In particular, we found that the filter-patches respond in an almost identical manner at high

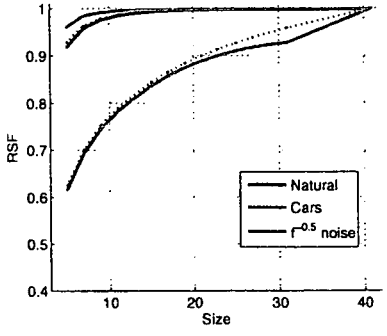


Figure 3. Average RSF curves for the different image ensembles tested. Blue: natural. Orange: cars. Green: random $f^{-0.5}$ noise. Solid lines represent the RSF curves obtained experimentally. Dotted lines indicate the theoretical curve predicted by eq. (12). The theoretical curves overlap with the experimental ones for the natural and car ensembles. The discrepancy between the theoretical curve and the experimental curve for the random $f^{-0.5}$ noise images for the higher resolutions is due to the fact we did not take into consideration the down-sampling. We observe that as the resolution is reduced, the RSF curves remain at about 1 for the natural and car images, until the resolution reaches about 15 pixels and 10 pixels respectively, beyond which the curves begin to drop. For the random images, in contrast, the RSF curve begins to drop at the onset of resolution reduction.

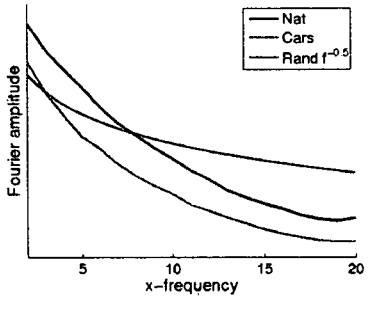


Figure 4. Cut of the log-amplitude spectra $\mathbf{Q}_{s_0}$ along the y-frequency 0, for the different image ensembles. Blue: natural. Orange: cars. Green: $f^{-0.5}$random noise. x-axis: horizontal frequencies. y-axis: log of the amplitude spectrum. The curve for the noise ensemble was translated vertically for presentation. The high frequencies are more dominant for the random images, implying the RSF function falls off more sharply as the resolution is reduced (Figure 3).

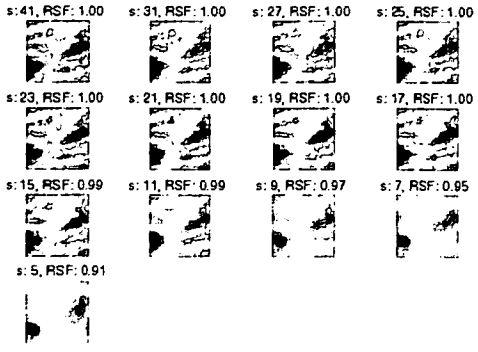


Figure 5. Examples of RSF values obtained for different sizes of a natural image patch filter. The RSF value is given for each size of the filter. For the display, the patches were not down-sampled. The RSF begins to drop after the resolution passes below a size of 15 pixels.

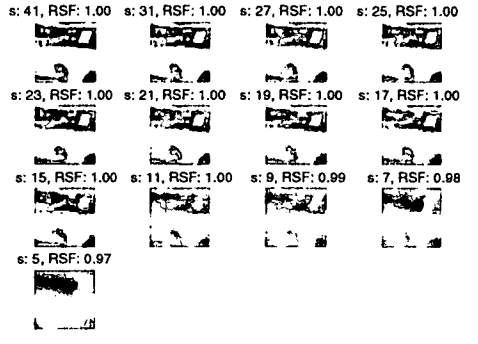


Figure 6. Car image ensemble. Examples of RSF values obtained for different sizes of a patch filter. The RSF drops when the resolution is below 11 pixels.

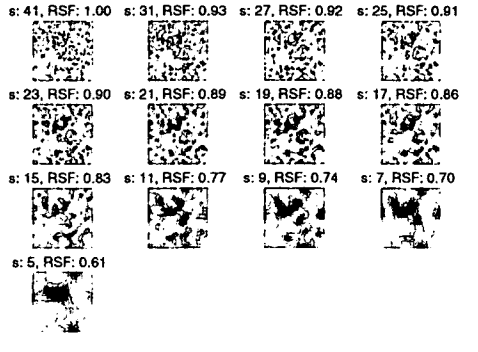


Figure 7. $f^{-0.5}$ noise images. Examples of RSF values obtained for different sizes of a $f^{-0.5}$ patch filter . We observe there is no resolution limit, the RSF value drops at the onset of resolution reduction.

resolutions (41x41 pixels) and at reduced resolutions, up to the limit of about 15x15 pixels for natural images and 10x10 pixels for the cars. In contrast, the responses of patches from a random noise image ensemble, where the lower frequency components of the images are less dominant, were significantly affected at the onset of resolution reduction.

First, the results suggest a basic lower limit resolution for the initial filter measurements in computer vision applications, because the responses of patches at higher resolutions, providing in principle more visual information, are actually fully explained by the responses of patches represented at the lower resolution limit. The resolution limits we found in our examples imply that features with a richer frequency content than Gabor type filters, derived by different encoding principles [10, 2], can be effectively used to extract information from the visual environment. Such features are shown in Figures 5 and 6. Reducing the resolution further leads to a deterioration of the responses and thereby a loss of information about the visual world. We can note that our result is in line with recent physiological studies, that suggest that primary visual cortex neurons may represent more complex stimuli than simple Gabors [14, 11].

Secondly, these results suggest that numerous computer vision applications using correlation based operators may benefit, in terms of computational complexity, from reducing the resolution of the filters down to the lower resolution limits that depend on the image statistics. More generally, the results suggest a method to incorporate prior knowledge about the image statistics, that can be used in learning applications. For example, in recognition methods that are based on selecting useful visual features with an exhaustive search through a large set of image patches, as in [21, 1, 18], the lower resolution limit can reduce the size of the feature search space.

We can mention several difficulties with our method that should be addressed. First, although we can clearly observe a cut-off in the car and natural image curves shown in Figure 3, it is not clear where to place the limit resolution exactly. In our experiments, we determined limit resolutions by an arbitrary RSF threshold of 0.99, but a more appropriate way would be to determine the threshold in an application dependent manner. Second, it is not clear whether the value of the initial feature size, 41x41 pixels here, will affect the RSF curves significantly. This is not expected, however, due to the scale-invariance properties of natural image ensembles [13]. Finally, the method for comparing the patch responses at different resolutions (eq. 2) may be critical for determining the resolution limits. For example, the comparison could be performed by computing the Mutual Information (MI) between the Patch Response Vectors (Section 3), rather than using NCC. MI can, in principle, capture more complex dependencies between random variables than can NCC. However, the use of MI would raise other issues, such as how to determine the binning. NCC is a straightforward method for comparison that captures the essential common

properties of two random vectors, and leads to a simple theoretical analysis.

In conclusion, we found a rough limit resolution for image patches when they are used as a first stage in the processing of natural scenes and object images. This limit depends solely on the spectral statistics of the image ensemble. Using higher resolution patches would not be more informative because their response properties do not differ significantly from the responses of patches at the lower limit resolution. We also found that the features of the limit resolution are more complex than simple Gabor type features, commonly used in computer vision applications, suggesting that more complex features can be effectively used in the first stages of visual processing. Finally, our results and analysis suggest that knowledge about image ensemble spectral statistics can be incorporated into applications requiring learning, such as object recognition, in order to simplify the computational complexity of the algorithm and facilitate the learning stage. This will be tested in future work.

## References


[1] S. Agarwal, A. Awan, and D. Roth. Learning to detect objects in images via a sparse, part-based representation. *IEEE Transactions on Pattern Analysis and Machine Intelligence*, 26(11):1475–1490, 2004. 1, 5

[2] A. J. Bell and T. J. Sejnowski. The 'independent components' of natural scenes are edge filters. *Vision Research*, 37(23):3327–3338, 1997. 5

[3] G. Dorkó and C. Schmid. Selection of scale-invariant parts for object class recognition. In *Proceedings of the International Conference on Computer Vision*, pages 634–640, 2003. 1

[4] B. Epshtein and S. Ullman. Feature hierarchies for object classification. In *Proceedings of the International Conference onComputer Vision*, pages 220–227, 2005. 1

[5] R. Fergus, P. Perona, and A. Zisserman. Object class recognition by unsupervised scale-invariant learning. In *Proc. of the IEEE Conf on Computer Vision and Pattern Recognition*, 2003. 1

[6] T. Kadir and M. Brady. Scale, saliency and image description. *International Journal of Computer Vision*, 45, 2001. 1

[7] D. G. Lowe. Distinctive image features from scale-invariant keypoints. *International Journal of Computer Vision*, pages 91–110, 2004. 1

[8] B. Lucas and T. Kanade. An iterative image registration technique with an application to stereo vision. In *Proceedings of the 7th International Joint Conference on Artificial Intelligence*, pages 674–679, 1981. 1

[9] J. Mutch and D. G. Lowe. Multiclass object recognition with sparse, localized features. In *Proceedings of the 2006 IEEE Computer Society Conference on Computer Vision and Pattern Recognition*, volume 1, pages 11–18, 2006. 1

[10] B. Olshausen and D. Field. Emergence of simple-cell receptive field properties by learning a sparse code for natural images. *Nature*, 381:560–561, 1996. 5

[11] B. Olshausen and D. Field. How close are we to understanding v1? *Neural Computation*, 17:1665–1699, 2005. 5

[12] C. Papageorgiou, M. Oren, and T. Poggio. A general framework for object detection. In *Proceedings of International Conference on Computer Vision*, 1998. 1

[13] D. L. Ruderman and W. Bialek. Statistics of natural images:scaling in the woods. *Phys. Rev. Lett.*, 73:814–817, 1994. 1, 3, 4, 5

[14] N. C. Rust, O. Schwartz, J. Movshon, and E. Simoncelli. Spatiotemporal elements of macaque v1 receptive fields. *Neuron*, 46:945–956, 2005. 5

[15] H. Schneiderman and T. Kanade. Probabilistic modeling of local appearance and spatial relationships for object recoognition. In *Proc. of the IEEE conference on Computer Vision and Pattern Recognition*, July 1998. 1

[16] S. Smith and J. Brady. SUSAN - a new approach to low level image processing. *Int. Journal of Computer Vision*, 23(1):45–78, May 1997. 1

[17] M. J. Swain and D. H. Ballard. Color indexing. *International Journal of Computer Vision*, 7:11–32, 1991. 1

[18] A. Torralba, K. Murphy, and W. Freeman. Sharing features: efficient boosting procedures for multiclass object detection. In *Proc. of the IEEE Conf on Computer Vision and Pattern Recognition*, pages 762–769, 2004. 1, 5

[19] A. Torralba and A. Oliva. Statistics of natural image categories. *Network: computation in neural systems*, 14:391–412, 2003. 1, 3, 4

[20] M. Turk and A. Pentland. Eigenfaces for recognition. *Journal of Cognitive Neuroscience*, 3:71–86, 1991. 1

[21] S. Ullman, M. Vidal-Naquet, and E. Sali. Visual features of intermediate complexity and their use in classification. *Nature Neuroscience*, 5:682–687, 2002. 1, 5

[22] J. van Hateren and A. van der Schaaf. Independent component filters of natural images compared with simple cells in primary visual cortex. *Proc.R.Soc.Lond. B*, (265):359–366, 1998. 2

[23] P. Viola and M. Jones. Rapid object detection using a boosted cascade of simple features. In *Proceedings IEEE Conf. on Computer Vision and Pattern Recognition*, 2001. 1

ELSEVIER

Journal of Neuroscience Methods 168 (2008) 140–145

JOURNAL OF NEUROSCIENCE METHODS

www.elsevier.com/locate/jneumeth

Short communication

# Optical filtering removes non-homogenous illumination artifacts in optical imaging

Andrzej W. Przybyszewski [a,*], Takayuki Sato [b], Mitsuhiro Fukuda [b]

[a] *Laboratory for Cortical Organization and Systematics, Brain Science Institute, RIKEN, 2-1 Hirosawa, Wako-shi, Saitama 351-0198, Japan*
[b] *Laboratory for Integrative Neural System, Brain Science Institute, RIKEN, 2-1 Hirosawa, Wako-shi, Saitama 351-0198, Japan*

Received 8 March 2007; received in revised form 7 August 2007; accepted 7 September 2007

**Abstract**

Under constant light illumination, cortical neuronal activity slightly modulates intensity of the light reflected from cortical surface. Optical imaging of the reflected light from the cortex has now become a popular method to obtain cortical functional maps. Since the modulation signal is small, this method is very sensitive to other sources of the light intensity changes. A well-known artifact in this signal is the bias in the reflected light intensity due to the curvature of the cortex. The curvature of the cortex creates inhomogeneity in reflected light intensity with characteristic concentric-ring pattern in the functional maps (known as ring-shape artifact). It is particularly visible in single-condition maps if the number of trials is small.

We demonstrate a method that can remove this and similar artifacts using an optical filter to equalize the reflected light intensity. Functional images recorded with the application of our filter – inserted into the optics between the cortex and the camera – became more uniform and distortion-free.

Our approach consisting of the equalization optical filter is appropriate for experiments where inhomogeneous light reflection, single-condition maps, and a small number of trials exist, e.g. imaging studies of higher cortices in behaving monkeys.


*Keywords:* Intrinsic signal; Ocular dominance column; Orientation column; Cortex; CBV; Cellular swelling

## 1. Introduction

Optical intrinsic signal imaging (OISI) is based on the fact that changes in the activity of local population neurons alter light absorption by the tissue (Blasdel and Salama, 1986; Bonhoeffer and Grinvald, 1996). The data analysis is performed once the digital images have been obtained from the camera. The camera is an intermediate step that converts the analog light signal (reflected light) into a digital image using an analog-to-digital (A/D) converter. To prevent saturation, the A/D converter must have a dynamic range greater than the range of the analog signal. The range of the analog signal for non-uniform light intensity is higher than that for uniform light. Also, the grayscale-resolution is inversely related to the range of the analog signal. The curvature of the cortex introduces changes in the reflected light intensity and therefore makes it non-uniform. As a result, the reflected light intensity suffers from poor grayscale-resolution upon digitization. Furthermore, the reflected light intensity is only modulated if the number of trials is small or single-condition experimental design (i.e., test images vs. control images) is used, ring-shaped artifact will be present and distort activation patterns in the images. In the present paper, we describe a novel method to remove static inhomogeneity in the reflected light intensity by means of an optical filter. As an example, we employ the optical filter to remove ring-shaped artifacts from the functional columnar maps.

## 2. Material and methods

### 2.1. Animal preparations

OISI was performed on three hemispheres in two Rhesus monkeys (*Macaca mulatta*). These animals had been used previously for OISI from the inferotemporal cortex. The surgery and recording procedures have been described in detail in a previous study (Li et al., 2003). Briefly, paralyzed monkey (vecuronium

* Corresponding author at: Department of Psychology, McGill University, 1205 Dr. Penfield Avenue, Montreal, QC H3A 1B1, Canada.
Tel.: +1 514 398 6151; fax: +1 514 398 3255.
*E-mail address:* przy@ego.psych.mcgill.ca (A.W. Przybyszewski).

0165-0270/$ – see front matter © 2007 Elsevier B.V. All rights reserved.
doi:10.1016/j.jneumeth.2007.09.006

bromide; 0.1 mg/(kg h), i.v.) was ventilated with isoflurane in a mixture of 70% $N_2O$ and 30% $O_2$. Craniotomy and duratomy were carried out inside an implanted chamber to expose the cortical surface. EEG was monitored to maintain a proper anesthetic level throughout the experiments. The temperature was maintained $37.8 \pm 0.2$ °C, and end-tidal $CO_2$ $4.5 \pm 0.5$%. All experimental procedures were done in accordance with the guidelines of the RIKEN Institute.

### 2.2. Visual stimuli

During the stimulus-on period, one of the four moving oriented square-wave gratings (1–3 cycle/degree; 0.5° $s^{-1}$; white: 8 cd/$m^2$, black: 0 cd/$m^2$; 0°, 45°, 90°, or 135°) was presented for 2 s to one eye by using eye shutters. As a control (no stimulation) OISI was recorded when both eye shutters were closed. Altogether, there was one control stimulus trial as described above, and eight test stimulus trials with four different orientations. We will refer to a 'trial' as one stimulus epoch (i.e., 1 s pre-stimulus period plus 3 s post-stimulus period).

### 2.3. Imaging systems

#### 2.3.1. Optics

Modified tandem-lens optics was used for this study (Fig. 1). An optical filter was placed in the first imaging plane of the lower tandem-lens (50 mm, f1.2, Nikon) and the charge coupled device (CCD) camera was placed in the second imaging plane of the upper tandem-lens (25 mm, f0.95, CCTV, Japan). Without the filter, the modified system works similarly to the standard tandem-lens optics. Optical filters were designed separately for each region-of-interest (ROI) of the cortex (Fig. 2A). The filter was made by inverting light intensity image of the cortex that would equalize the reflected light intensity. The camera was focused at the location below the cortical surface from where the intrinsic signal was recorded. A single frame image at this depth was taken (Fig. 2B), saved and processed by Photoshop (Adobe) software, where its intensity was inverted. The inverted image with adjusted mean light intensity on Photoshop was printed in the scale 1:1 on a transparency. This transparency formed the optical filter. An example of the optical filter image is shown in Fig. 2C. In the next step, the filter was placed in the filter frame and inserted into the filter positioner to move into an appropriate $x$-, $y$-, and $z$-position, and another picture of the cortex through the filter was taken (Fig. 2D). The filter must fit the image of the cortex precisely to compensate for the static inhomogeneity in the reflected light. This was achieved by moving the filter in the $x$- and $y$-direction in such way that when pial vascular patterns on the cortex matched those on the filter, the pial vasculatures patterns become invisible in the acquired image. Moving the filter in $z$-direction changes the position of the filter relative to

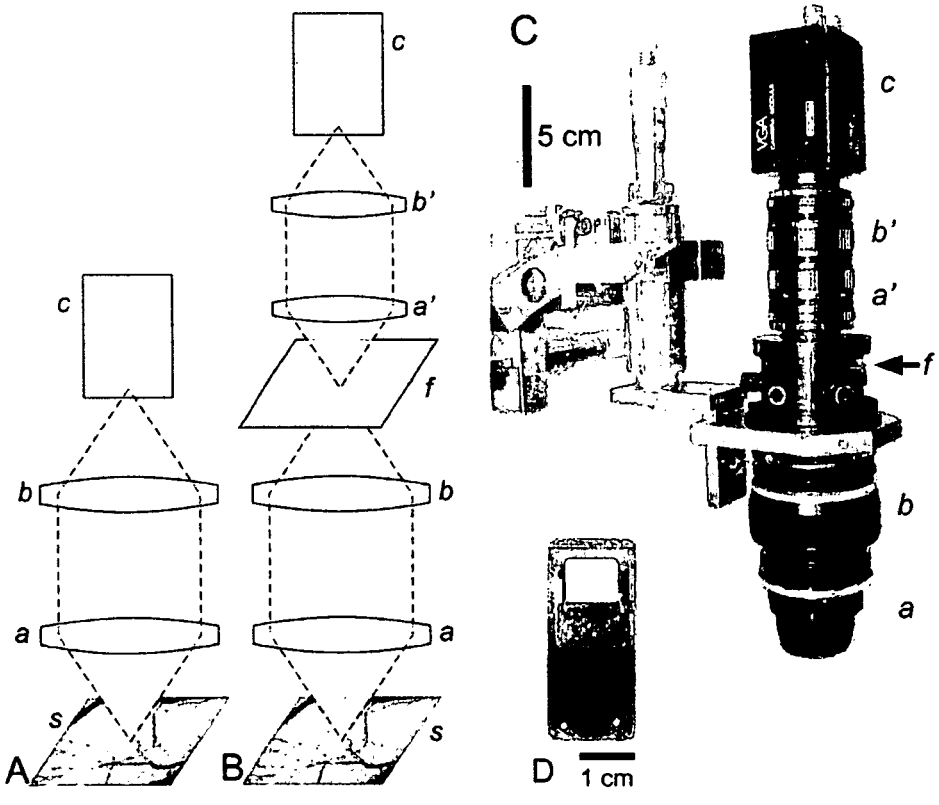


Fig. 1. Commonly used tandem-lens optics for OISI vs. modified optics with the photography of the modified system. (A) Schematics of tandem-lens between cortex and camera in the standard recording system. (B) Schematics of lens and filters between cortex and camera in the modified recording system. The filter was placed in the position of the camera in A, and another tandem-lens system was built between filter and the camera. Abbreviations: s, cortical surface; a and a', objective lenses; b and b', projection lenses; c, CCD camera; f, optical filter. (C) The modified lens system with the CCD camera attached to the micromanipulator. In order to decrease system size, in the set between filter and camera a smaller size lenses were used. (D) Frame with the window for the filter.

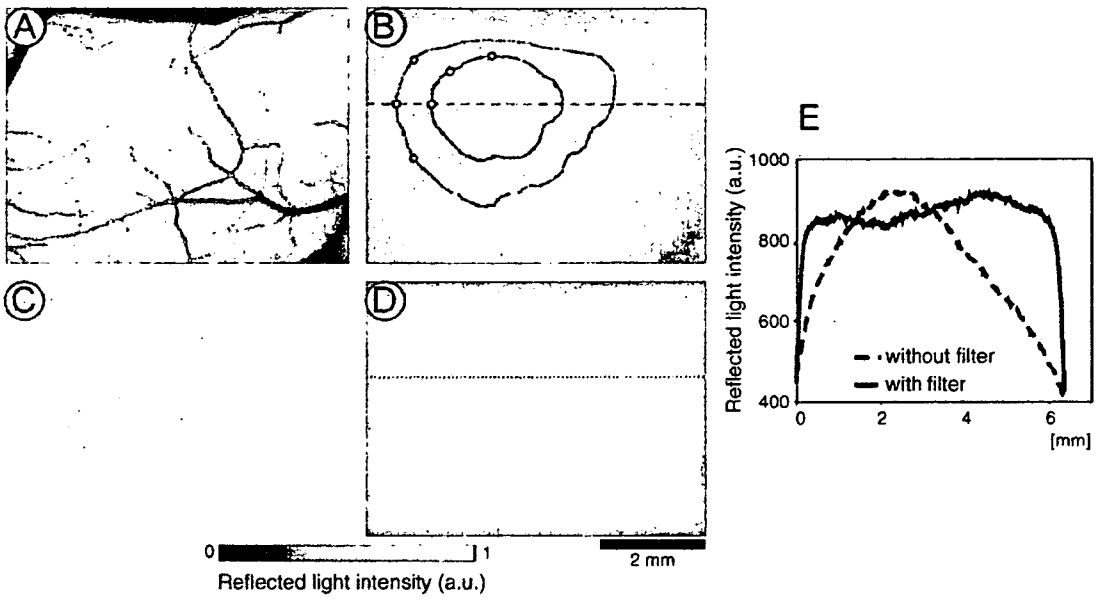


Fig. 2. The correction of inhomogeneity of reflected light intensity with the optical filter. (A) Cortical surface image (green, 540 nm wavelength light illumination). (B) Image of the cortex at the depth of 700 μm below the surface (607 nm illumination); maximum changes in the light intensity are near the upper left corner of the image. Along dotted line intensity profile was analyzed and presented on panel E. Colored dots representing the ring-shape artifacts were added to this image in the same location as in Fig. 4A–C. When dots with the same color were connected, they determined equiluminance rings showed in the image. (C) Image of the filter that was created by inversion of the cortical image (compare to B). (D) Image of the cortex with the filter (compare to B). Along dotted line intensity profile was analyzed and presented in panel E, a.u.: arbitrary unit. (E) Comparisons of light intensity profiles with and without an optical filter (dotted line). A profile of the cortical image taken without filter along the line shown in part B (solid line). A profile of the cortical image taken with filter along the line shown in panel D. (For interpretation of the references to color in this figure legend, the reader is referred to the web version of the article.)

the focal plane. It blurs the image or introduces a low-pass spatial frequency filtering which is necessary to remove the texture of the filter. The adjustments of the filter position are necessary for the functioning of the system. The image intensity of the cortex became more uniform as a result of the static artifacts compensation (compare Fig. 2B and D).

### 2.3.2. *Optical intrinsic signal imaging*

The exposed cortical surface was illuminated using light of wavelength of either 540 ± 10 nm (pial vessel image) or 607 ± 10 nm (OISI). Images were obtained using a CCD camera (640 × 480 pixels; CS8310, Teli, Japan) and digitized with a 10-bit video A/D converter board (Pulsar, Matrox Graphics Inc., Canada) connected to the PCI bus of IBM PC. The area imaged was 6.4 mm × 4.8 mm and after spatial averaging of the pixels (2 × 2 binning), it contained 320 × 240 pixels. For the OISI recording, the focusing depth was adjusted to 700 μm below the cortical surface rather than 300 μm commonly used for optical imaging of intrinsic signal. The purpose of imaging the cortical surface out-of-focus is to mitigate the artifact from pial vessels in the generated maps (Bonhoeffer and Grinvald, 1993). Empirically, we have learned that the 300 μm in contrast to 700 μm out-of-focus is frequently not sufficient to avoid pial vessel artifact in differential maps. The differential maps obtained at 0–1000 μm are essentially the same except for the vessel artifacts. We did not systematically study relationships between appearance of ring-shaped artifacts and focal plane. As long as the global inhomogeneity of the reflected light intensity is present, the ring-shape artifacts will also be observed.

The data acquisition started at a certain phase of respiration in synchrony with heartbeat and continued for 4 s for each stimulus (one trial). Each image was acquired at the rate of 0.5 s per image. Stimulus-on period started 1 s after the onset of data acquisition and continued for 2 s. Inter-stimulus intervals (stimulus offset to onset) were set to 8 s. The period of illumination was restricted to 8 s by a mechanical shutter that opened 2 s before the data acquisition. For each oriented grating, stimulus was presented 20 times to each eye; thus altogether each eye was stimulated 80 times.

### 2.4. *Data analysis*

A pre-stimulus baseline image was obtained by averaging images taken during 1-s period just before the stimulus started. The percent signal change (first frame analysis) was done by dividing the difference images (stimulus images minus the pre-stimulus baseline image) by the pre-stimulus baseline image (Bonhoeffer and Grinvald, 1996). The resulting percentage signal change for each image (during 2.5 s including 0.5 s delay after the stimulus onset) was then averaged to obtain a single-condition activity map for each stimulus (i.e., four orientations and one blank for each eye).

Below, we will define: single-condition ocular dominance map and differential ocular dominance map, which were used in our analysis. Single-condition ocular dominance map was

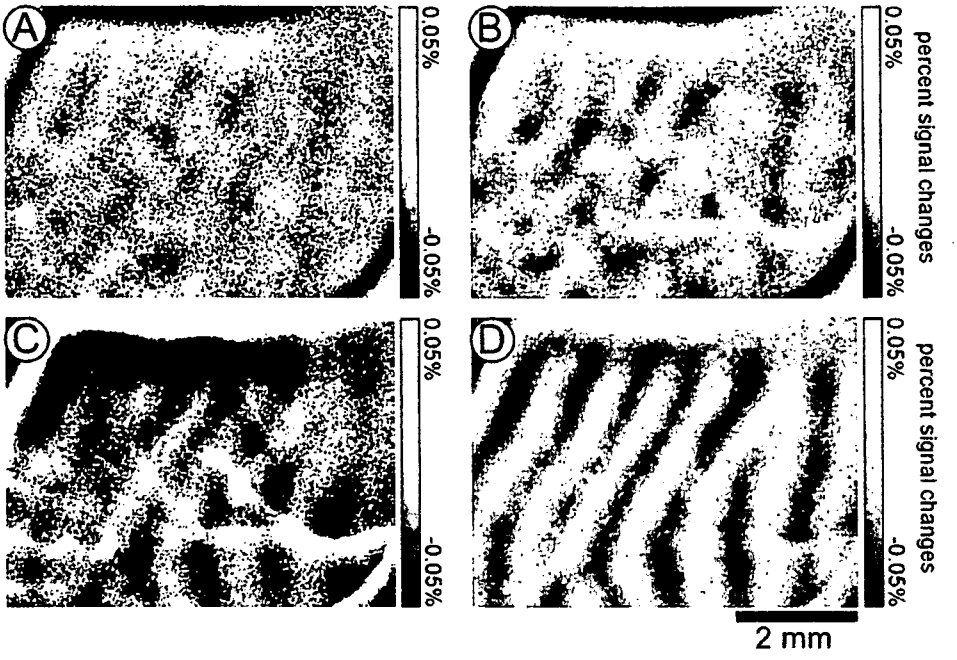


Fig. 3. Comparisons between single-condition ocular dominance map and differential ocular dominance map without optical filter. (A) Averaged single-condition ocular dominance map of the first eight trials during left eye stimulation. Notice ring-shaped artifacts around maximum intensity of illumination. (B) Averaged single-condition ocular dominance map of 80 trials during left eye stimulation. (C) Averaged differential ocular dominance map of the first eight trials obtained by subtracting the responses to left eye stimulation from those to the right eye stimulation. (D) Averaged differential ocular dominance map of 80 trials.

calculated for each eye by subtracting the single-condition activity map for blank stimulus from the averaged single-condition activity map for four-orientation stimulation. Differential ocular dominance map was calculated by subtracting the single-condition ocular dominance map of one eye from that of the other eye.

A Gaussian band-pass spatial filter (cutoff frequencies were 20.4 $mm^{-1}$ for the high and 0.3 $mm^{-1}$ for the low range) was used to enhance the contrast of ocular dominance columns of the single-condition ocular dominance map, the differential ocular dominance map and a single-condition activity map for one orientation shown in Fig. 4C. Notice that the ring-shaped artifacts are in the narrow frequency range between 5 and 10 cycle/mm and therefore, they are not affected by the Gaussian band-pass spatial filter (Malonek and Grinvald, 1996). Pixels with the same luminance intensity were extracted with help of the IDL software and used to draw the contours (see Fig. 2B).

Ring-shaped artifacts were observed in all three hemispheres that were studied. In the following section we will present experimental results obtained from one hemisphere, in which the ring-shaped artifacts were most clearly visible.

## 3. Results

To examine the ring-shaped artifacts, we performed OISI using the conventional tandem of the optical lens (see Fig. 1A). A curved surface of the cortex introduced inhomogeneity in the reflected light from the ROI (see Fig. 2B). In the single-condition ocular dominance map, obtained by averaging the responses from eight trials (Fig. 3A), ring-shaped artifacts are clearly visible. These artifacts distort the ocular-dominance-columns pattern and are still noticeable even after averaging the responses from 80 trials (Fig. 3B). However, in the differential ocular dominance map, obtained by averaging the responses from eight trials, the ring-shaped artifacts were not clearly noticeable (Fig. 3C). After averaging the responses from 80 trials, the artifact was completely eliminated (Fig. 3D). It should be noted that ring-shaped artifacts appear to be similarly observed in the control image (not shown). Nevertheless, we have also observed this artifact in the single-condition ocular dominance map.

A more detailed analysis of the images containing the ring-shaped artifacts was performed (Figs. 2 and 4). Red and green markers were placed on the same ring-shaped artifacts in the single-condition ocular dominance map averaged from the eight trials (Fig. 4A). The markers were also placed in the same position in another averaged single-condition ocular dominance map shown in Fig. 4B (eight trials containing clear visible ring-shaped artifacts), and in a single-condition activity map for one orientation (Fig. 4C). The rings seemed to stay nearly at the same positions relative to the markers across different trials. Thus, neither simple averaging of responses nor comparisons of test-stimulus-response and control-stimulus-response seemed to diminish the ring-shaped artifact in functional maps. Dots with the same color turned out to have an identical light level intensity (Fig. 2B). Therefore, we assumed that the ring-shaped artifacts are linked to the inhomogeneity in the light reflected from the cortex.

In order to remove this inhomogeneity we used an optical filter mounted between lenses. Two light intensity profiles

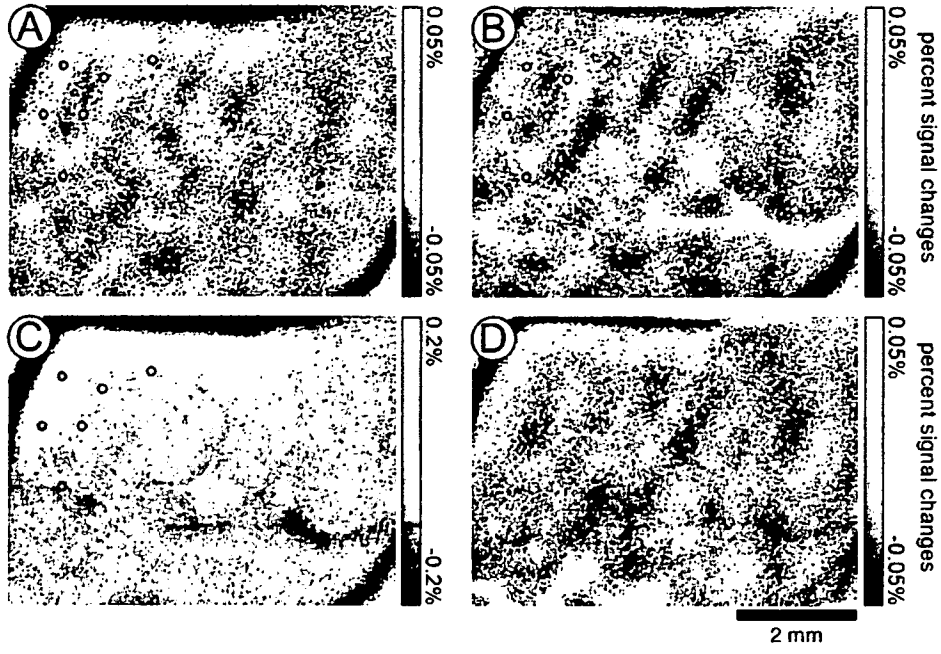


Fig. 4. Consistent appearance of the ring-shaped artifacts removed by introduction of the optical filter. (A) The single-condition ocular dominance map from Fig. 3A with red and green dots placed on two different ring-shaped artifacts. (B) This image is also averaged of the single-condition ocular dominance map, but eight trials with prominent ring-shaped artifacts were selected. Notice that in both images (A and B) ring-shaped artifacts are similar. (C) A single-condition activity map of one-trial recording. This image represents the response to vertical grating. (D) Averaged single-condition ocular dominance map of the first eight trials during left eye stimulation registered in the exactly same conditions as in Fig. 3A but with the optical filter. (For interpretation of the references to color in this figure legend, the reader is referred to the web version of the article.)

of the cortical images are shown in Fig. 2E. The first profile (dotted line) was obtained from a control image recorded without the filter along the dotted line in Fig. 2B. It shows large spatial variability of the intensity. The intensity appears to gradually increase from the peripheral towards the central portion of the image. The second intensity profile (solid line in Fig. 2E) was obtained from the filtered image and along the same line (Fig. 2D). The light intensity profile of the central portion of the filtered image is nearly uniform. Although a considerable decrease in the light intensity is present at the image edge, this affects a relatively small portion of the image area and lies outside the ROI. These differences in intensity profiles strongly influence OISI. The single-condition ocular dominance map obtained by averaging of eight trials (Fig. 3A) was computed in the same experimental conditions but with the optical filter (Fig. 4D). In the last experiment, the ring-shaped artifacts were removed because of the optical filter. We have obtained similar improvements in all three hemispheres in the two monkeys.

## 4. Discussion

We have showed using a simple example that the optical filter completely removed ring-shaped artifacts caused by global illumination inhomogeneity. This inhomogeneity can be corrected by the division of pre-stimulus image (i.e., first frame analysis, Bonhoeffer and Grinvald, 1996). However, this correction does not diminish ring-shape artifacts as seen in our single-condition maps. Introduction of the optical filter makes the reflected light intensity profile flat for locations within the boundary of the cortex (central portions of the image). The values of the intensity (central portions of the image) have similar magnitude when compared to the maximum light intensity in the non-filter case (Fig. 2E). For this reason and by direct comparison of the images with and without the filter (data not shown) we think that the intrinsic signal is at least as strong with filter as without. Furthermore, the intrinsic signal is no longer affected by the ring-shape artifact; therefore the ocular dominance map is clearer and more uniform with the filter than without it (Fig. 4). We increased the incident illumination when using the filter so that the CCD camera receives the same reflected light intensity with and without the filter. However, we do not think that an increase in illumination alone could account for the improvement or for the cortex damage because the amplitude of the intrinsic signal is similar with and without the filter (compare Fig. 3A and Fig. 4D).

When observing the ring-shaped artifacts in Fig. 2B and comparing them with the intensity profile (Fig. 2E), we found that these artifacts were observed in the areas with a large gradient of the light intensity. One hypothesis, which could explain the source of the ring-shaped artifacts, is related to the digitization levels of the A/D converter. We used 10-bits A/D converter with 1024 digitization levels. In consequence our converter has precision about 0.1% of the signal amplitude, which is in the same range as our intrinsic signal. Therefore, changes in reflected light intensity due to movements of the cortical surface could introduce abrupt changes in the output signal and in consequence in the optical image. These changes will be more

pronounced in the area with large gradients of the light intensity and they may produce the ring-shaped artifacts. Also the reflected light intensity is influenced by brain movements possibly related to brain volume alterations due to stimulus-induced changes in cerebral blood volume and cellular swelling. In consequence, ring-shaped artifacts are reduced in the differential images but not in the single-condition images. Another possibility is interference of waves reflecting from two non-parallel surfaces. This effect is called Newton's Rings. In this case it is monochromatic light waves that are being reflected at cortical surface and silicon oil. Differences in the refractive index between two different materials (cerebral fluid vs. silicon oil) cause the light wave phase shift. They interact according to the distance between cortical surface and silicon oil. This distance is constantly changing because the convex surface of the cortex.

We have already tested our method in optical imaging from the inferotemporal cortex (see work from our lab: Sato et al., 2004; Uchida et al., 2002). The inferotemporal cortex presents several technical difficulties in the acquisition of intrinsic signals. First, due to the highly skewed shape of the inferotemporal cortex, the reflected light intensity is more inhomogeneous than in the other visual areas. Second, the magnitude of the intrinsic signals is generally smaller in inferotemporal cortex than in V1 cortical region (Tsunoda et al., 2001; Wang et al., 1996; Yamane et al., 2006). Third, in experiments involving the inferotemporal cortex, the patterns of stimulation are more complex (Fujita et al., 1992; Tanaka et al., 1991; Tsunoda et al., 2001) than gratings and "orthogonal" stimulation patterns are not known. Thus, in most cases, test conditions have to be compared with the control (i.e., blank screen); the conditions are similar to Fig. 3A than to Fig. 4C. Also our filter is more effective when applied to the optical imaging where only a small number of trials are possible. For example, when OISI is performed on behaving monkeys (Grinvald et al., 1991; Shtoyerman et al., 2000; Siegel et al., 2003; Vnek et al., 1999), the practical number of trials is significantly less than when anaesthetized animals are used. Furthermore, the intensity profile of the filtered optical image is essentially flat, and therefore, implies that the dynamic range of the analog signal is small. As a result, if the filter is used, the images can be digitized at a high resolution.

## Acknowledgements

We very much appreciate the technical assistance of Dr. Manabu Tanifuji for implementing the modified optics and his suggested comments on our manuscript. We thank Rahul Chander for his comments and help in editing the manuscript, and Miroslaw Jonasz for his suggestions regarding the possible causes of the ring-shaped artifacts.

## References

Blasdel GG, Salama G. Voltage-sensitive dyes reveal a modular organization in monkey striate cortex. Nature 1986;321:579–85.

Bonhoeffer T, Grinvald A. The layout of iso-orientation domains in area 18 of cat visual cortex: optical imaging reveals a pinwheel-like organization. J Neurosci 1993;13:4157–80.

Bonhoeffer T, Grinvald A. Optical imaging based on intrinsic signals: the methodology. In: Toga AW, Mazziotta JC, editors. Brain mapping: the methods. San Diego: Academic; 1996. p. 55–97.

Fujita I, Tanaka K, Ito M, Cheng K. Columns for visual features of objects in monkey inferotemporal cortex. Nature 1992;360:343–6.

Grinvald A, Frostig RD, Siegel RM, Bartfeld E. High-resolution optical imaging of functional brain architecture in the awake monkey. Proc Natl Acad Sci USA 1991;88:11559–63.

Li H, Fukuda M, Tanifuji M, Rockland KS. Intrinsic collaterals of layer 6 Meynert cells and functional columns in primate V1. Neuroscience 2003;120:1061–9.

Malonek D, Grinvald A. Interactions between electrical activity and cortical microcirculation revealed by imaging spectroscopy: implications for functional brain mapping. Science 1996;272:551–4.

Sato T, Uchida G, Tanifuji M. Nature of neuronal clustering in inferotemporal cortex of Macaque moneky revealed by optical imaging and extracellular recording. Soc Neurosci Abst 2004;34:300–12.

Shtoyerman E, Arieli A, Slovin H, Vanzetta I, Grinvald A. Long-term optical imaging and spectroscopy reveal mechanisms underlying the intrinsic signal and stability of cortical maps in V1 of behaving monkeys. J Neurosci 2000;20:8111–21.

Siegel RM, Raffi M, Phinney RE, Turner JA, Jando G. Functional architecture of eye position gain fields in visual association cortex of behaving monkey. J Neurophysiol 2003;90:1279–94.

Tanaka K, Saito H, Fukada Y, Moriya M. Coding visual images of objects in the inferotemporal cortex of the macaque monkey. J Neurophysiol 1991;66:170–89.

Tsunoda K, Yamane Y, Nishizaki M, Tanifuji M. Complex objects are represented in macaque inferotemporal cortex by the combination of feature columns. Nat Neurosci 2001;4:832–8.

Uchida G, Fukuda M, Sato T, Tanifuji M. Spike synchronization between functional columns in the inferotemporal cortex of anesthetized monkeys. Soc Neurosci Abst 2002;32, 160-113.

Vnek N, Ramsden BM, Hung C, Goldman-Rakic PS, Roe AW. Optical imaging of functional domains in the cortex of the awake and behaving monkey. Proc Natl Acad Sci USA 1999;96:4057–60.

Wang G, Tanaka K, Tanifuji M. Optical imaging of functional organization in the monkey inferotemporal cortex. Science 1996;272: 1665–8.

Yamane Y, Tsunoda K, Matsumoto M, Phillips AN, Tanifuji M. Representation of the spatial relationship among object parts by neurons in macaque inferotemporal cortex. J Neurophysiol 2006;96:3147–56.

生物物理 47 (6), 352-354 (2007)

ミニ特集　脳における情報処理：時間構造の中に情報を埋め込む

# ミニ特集に寄せて

谷藤　学　理化学研究所脳科学研究センター

脳は外界や身体の状態に関する情報（感覚情報）から必要なものを選択し，それをもとに行動を計画し，運動系に対して実行を指令する．いわば，感覚入力から運動情報への変換を行う多段の情報処理装置である．しかし，私たちの脳の働きは，「刺激-応答」の単純な連鎖だけでは説明できない．たとえば，この単純な枠組みで，1つの状態にとどまることのない私たちの意識や思考を説明できるとは思えない．脳の状態の時々刻々の変化，すなわち，神経活動のダイナミクスを考慮する必要がある．また，脳の活動状態はいろいろあって，それらの間を遷移するといい換えれば，物理学の問題としても面白い．そういうわけで神経活動のダイナミクスと情報表現の関係について考えてみたいのである．このミニ特集では，それを考える手がかりになるような神経科学の研究やそのレビューを4つ選んで特集する．なお，紙面の都合上取り上げることはできなかったが，物理学から見た脳における状態と遷移の問題についてはよい総説[1]があるのであわせて参照されたい．それぞれのトピックに入る前に，それぞれをどういう意図で取り上げたか少し解説しておこう．

**1. 神経細胞の同期発火と行動：カエルの逃避行動に網膜細胞の同期した周期発火が本質的な役割を果たす (p. 355)**

神経活動のダイナミクスという言葉から，神経細胞の同期発火現象を思い浮かべる人も多いに違いない．これまで同期発火に関しては多くの研究があるが，それが実際に機能的な役割をもっているかということについては議論がある．同期発火が脳における情報処理に本質的であるというためには，同期発火を観測するだけではだめで，同期発火を生成するメカニズムと下流にある細胞や最終的なアウトプットである行動に同期発火がどのような効果を及ぼすかまでを明らかにしなければならない．しかし，多くの場合，同期発火の観測はあっても，生成メカニズムとその効果については推測以上のものがなく，そのことが議論を引き起こす原因となっている．本特集では，カエルの逃避行動という系でこの3つの要素をきちんと扱った研究を取り上げた．

**2. 神経細胞の膜電位がもつ双安定性と状態遷移：その仕組みと情報処理における役割 (p. 362)**

生きている動物（哺乳類）から単一細胞の膜電位を直接計測するという難しい実験が可能になって，静止状態にある細胞の膜電位がアップとダウンの2つの安定した状態をとることがだんだんわかってきた．アップは細胞が発火しやすい状態（脱分極電位で安定）で，ダウンは細胞が発火しにくい状態（過分極電位で安定）である．細胞レベルで起こるこの2つの状態の間のゆらぎは，情報表現と何か関係しているのだろうか？　私たちの認知的な行動には1つの安定な状態から別の安定な状態に遷移しているように見えるものがある．たとえば，1つのところに向けられた「注意」はしばらくそこにあって，突然，別のところに移る．もし細胞レベルのアップとダウンの状態間ゆらぎがこのような行動レベルの状態遷移と関連しているとしたらたいへん面白い．残念ながらその証拠は今のところなく，その生理学的な意味についてもまださまざまな議論がある．この新しいタイプの神経活動のダイナミ

Foreword to a Mini-Assembly of "Temporal Structure and Dynamics of Neural Activity: How They Relate to Information Processing in the Brain?"
Manabu TANIFUJI
RIKEN Brain Science Institute

クスについて何がどう問題になっているのか知っておく価値があると考えて取り上げた.

### 3. メモリーリプレイと記憶の固定化（p. 368）

記憶はいうまでもなく脳の重要な機能の1つである. その記憶をしっかり定着させるためには, 行動中に海馬のシナプスレベルで起こる可塑的な変化だけでは不十分で, 睡眠中に連合皮質にその記憶を定着させるプロセスが必要であると考えられている. さて, 記憶される情報は, 多くの場合, いくつかのイベントが時間的に並んだひとつながりのエピソードになっていることが多い. このような時間構造をもつエピソードを定着させるためのメカニズムとして, メモリーリプレイという考え方がある. まず, 一連の行動を行って

いるときには，その行動の要素の順番にしたがって，海馬においてそれぞれの要素に関連する一連の神経細胞が順に活動し，その順番にしたがってシナプスの強化が起こる．次に，睡眠中自発的にこれらの神経細胞が活動すると，強化された順にしたがって，順番に神経細胞が活動するだろう．この一連の神経細胞の活動（メモリーリプレイ）が皮質連合野への指令となって，皮質連合野の可塑性を引き起こす．この仮説に対して，多くの研究者が挑戦しているが，まだ，確証を得るにはいたっていない．1つの難しさは，睡眠中に観測されるリプレイが偶然的に生じたものではなく，確かにリプレイであると確信することであろう．手がかりは，活動の順番が行動中に起こる活動の順番と一致しているということしかなく，また，睡眠中の自発的な活動のすべてが着目しているエピソードのリプレイではないからである．いわば稀現象の観測なのである．神経活動のダイナミクスが脳の機能とかかわる1つのあり方として，この問題がどこまで明らかになったのか取り上げてみたいと考えた．

### 4. 多義的知覚の心理物理計測から推測される離散的な脳内過程（p. 378）

さて最後は「意識」の問題である．客観的に計測することができないのでその脳内機構を解明することは一般的には難しいが，1つの切り口として着目されているのが視覚的意識の問題である．この視覚的意識の意味は本論文に譲るとして，興味深いのは，この視覚的意識の研究においては意識の時間的なゆらぎを定量的に計測できることである．視覚的意識のゆらぎのダイナミクスの定量的な解析からどこまで，その脳内メカニズムに迫れるだろうか？

以上がこの特集を企画した意図である．はじめに述べたように，4つのトピックは必ずしもリンクされてはいない．むしろこの特集を通して，生物物理の読者に，神経活動の時間構造と情報表現を考える一助にしてほしいと考えている．そのために，執筆はそれぞれのトピックに直接かかわっている優れた研究者にお願いした．しっかりとした議論が展開されているので役に立つものと思う．忙しい中，無理をいって執筆をお願いした著者の皆様にはこの場を借りて特にお礼を申し上げます．

### 文 献

1) 大沢文夫 (2001) 自主，自発と個体差，「複雑系のバイオフィジックス」，pp. 155-192，共立出版，東京．

谷藤 学

**谷藤 学（たにふじ まなぶ）**
理化学研究所脳科学総合研究センター チームリーダー
生理学研究所助手，福井大学助教授を経て1996年より理化学研究所に勤務．国際フロンティア研究システム副チームリーダー，チームリーダーを経て97年より現職．
研究内容：視野に入ってくる物体像の脳内表現，処理，そして，物体像の認識にいたる過程を研究している．よい研究にはよい計測法が必要だと思っているので，脳表面の活動の空間パターンを捉えるための内因性信号のイメージング法，空間ばかりでなく時間パターンを計測できる高密度電極アレイ，脳表面の下にあって隠れた機能構造を捉える技術である機能的オプティカル・コヒーレンス・トモグラフィなどの技術を必要に応じて開発してきた．最近は，物体像の認識にもかかわってくる注意の機構や意識にも関心をもっている．
連絡先：〒351-0198 埼玉県和光市広沢2-1
E-mail: tanifuji@riken.jp

生物物理 47 (6), 362-367 (2007)

ミニ特集　脳における情報処理：時間構造の中に情報を埋め込む

# 神経細胞の膜電位がもつ双安定性と状態遷移：その仕組みと情報処理における役割

内田　豪　理化学研究所脳科学総合研究センター

Many studies reported that membrane potential of a neuron fluctuates between two stable states (depolarized 'up' state and hyperpolarized 'down' state). A neuron fires at the up state but rarely fires at the down state. Thus, the two states fluctuation is likely to influence information processing in the brain, because spike activity of a neuron conveys information in the brain. In this review, I will discuss possible functional roles and underlying mechanisms of the two states fluctuation.

**brain / information processing / membrane potential / two states fluctuation / non-linear dynamics / network dynamics**

## 1. はじめに

脳は多数の神経細胞からなる複雑なネットワークでできており，1つの神経細胞からの信号は軸索とよばれる長い神経線維を通って次の細胞へと伝えられる．この信号の実体は細胞の膜電位の変動であるが，長い軸索を減衰することなく伝わる変動は，パルス状の膜電位変化である活動電位だけである．したがって，脳における情報処理を理解するためには活動電位の時系列（発火系列）の性質を調べることが不可欠である．一般に神経細胞は規則的に活動電位を発生する（発火する）のではなく，発火のタイミングはゆらいでいることが多い．このことから，発火系列の性質を記述するためには確率過程論が有効である．実際の細胞の発火系列は，完全にランダムでポワソン過程を用いてよく近似できるものから，より不規則性の少ないものまでさまざまである．多くの場合，情報は発火系列の平均発火頻度の時間的な変化によって運ばれていると考えられているが，それに加えて発火のタイミングも情報伝達において重要であるという説もある．

さて，神経細胞の発火は，分極している膜電位が別の細胞の発火による入力を受けて脱分極し，ある閾値を超えると起こる．したがって，平均発火頻度の変化は膜電位変化のダイナミクスと密接な関係をもっている．そして，一般に膜電位は入力となる発火系列の平均発火頻度の変化などに応じて比較的連続に変化していると捉えられることが多い．しかし，ここ十数年来膜電位変化にさらに興味深いダイナミクスがあることがわかってきた．それが，ここで取り上げる膜電位の状態間ゆらぎである（**Fig. 1**）．

状態間ゆらぎは神経細胞の膜電位が2つの安定した状態の間をゆらぐ現象で，さまざまな動物のさまざまな脳の部位で観測されている．一般に，2つの状態のうち，より分極した状態をダウン状態，もう1つの状態をアップ状態とよぶ．状態間ゆらぎのダイナミクスは動物の種類，部位，動物の状態（麻酔下，自然な睡眠状態，覚醒状態），刺激の有無によってさまざまである．たとえばそれぞれの状態の平均持続時間は，条件によって数十 ms から数 s までの幅がある．また，周期性についても，数 Hz 以下の周期のまわりをゆらいでいる場合もあれば，特徴的な周期をもたない場合もある．しかし，いずれの場合にも共通した重要な性質として，細胞はアップ状態ではよく発火するが，ダウン状態ではまったく発火しないか，きわめて低い頻度でしか発火しないということがある．このことは，状態間ゆらぎが脳内の情報処理に大きな影響を与えうることを意味する．以下に記述するように，状態間ゆらぎの機能はまだ十分理解されているとはいい難いが，考えられる機能には興味

Bistability and State Transition in Membrane Potential of a Neuron: Their Functional Roles in Information Processing and Underlying Mechanisms
Go UCHIDA
Brain Science Institute, RIKEN

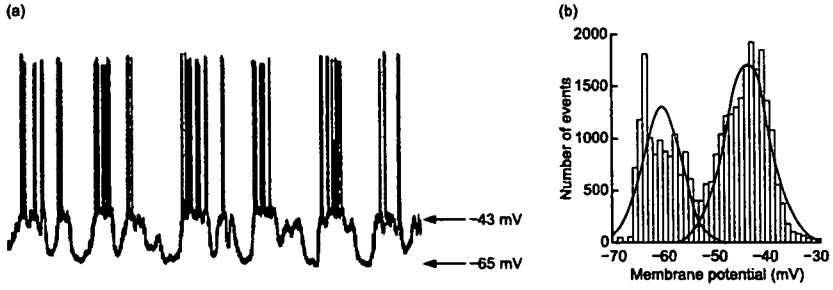


**Fig. 1**
Two states membrane potential fluctuation of a rat striatum neuron. (a) Intracellular trace for 6.4 s. Membrane potentials corresponding to the up and down states are labeled at the right ends of the trace. (b) Histogram of membrane potentials shown in (a). The histogram does not include the action potentials. The histogram shows clearly distinct two peaks that correspond to the up and down states. Adapted from ref. 1 and used with permission.

深いものが多い.

本稿では，状態間ゆらぎの機能と発生の仕組みについて現在までに明らかになっていることをまとめる．状態間ゆらぎの研究はさまざまな動物で行われている．最も興味深いのはヒトと同じ霊長類であるサルであるが，サルとそれ以外の動物とでは事情が大きく異なる．状態間ゆらぎを直接計測するためには，膜電位を直接計測する必要がある．一般に個々の細胞の膜電位を直接計測するためには，細胞内電気記録を行う必要があるが，これを *in vivo*（生体内）で行うことは基本的に難しい．したがって，実験に多くの手間を要する高等動物になるほど，その成功例は少なくなる．現在のところ，サル以外の動物（ラット，ネコなど）では困難を伴うものの *in vivo* での細胞内電気記録で膜電位の状態間ゆらぎを直接計測した研究がいくつかある．一方，サルでは著者の知る限り *in vivo* での細胞内電気記録の成功例はなく，より簡単な方法である細胞外電気記録（膜電位は計測できないが発火活動は記録可能）で記録された発火活動から数理モデルを通して状態間ゆらぎの存在を明らかにするというのが唯一の有効な方法である．そこで，本稿では状態間ゆらぎに関する研究をサル以外の動物とサルとに分けてまとめた．さらに，サル以外の動物に関しては，機能との関係を理解しやすいように脳の部位ごとに記述を行った．

## 2. サル以外の動物

状態間ゆらぎはラットやネコなどの脳のさまざまな部位で細胞内電気記録により直接観測されている．ここでは，状態間ゆらぎが観測される代表的な部位である線条体，小脳，大脳皮質を取り上げる．これらの部位のうち，線条体，小脳では状態間ゆらぎの機能に関する研究はほとんど行われていない．一方，大脳皮質では機能に関する研究がいくつか行われているが，研究により異なる結果が得られており，状態間ゆらぎの機能に関して意見の一致を見ていないのが現状である．また，状態間ゆらぎの仕組みに関しては，大脳皮質，小脳はそれぞれ独自の異なる仕組みをもっていると考えられている．一方，線条体はそれ自身で状態間ゆらぎを発生させる仕組みはもっておらず，大脳皮質からの入力をただ反映してゆらぎが起こっているにすぎないと考えられている．以下にそれぞれの部位について詳述する．

### 2.1 線条体

膜電位の状態間ゆらぎが最も古くから知られているのは，ラットの線条体（striatum）にある中型有棘細胞であろう．線条体は大脳基底核とよばれる神経細胞の集まりの主要な構成要素の1つである．大脳基底核は運動の制御にかかわっていることがよく知られており，パーキンソン病の患者では大脳基底核に病的な変化が認められる．大脳基底核は大脳皮質にあるほとんどすべての領野から入力を受けているが，その最初の受け手が線条体であり，中型有棘細胞が全体の90-95%を占めている．

ラットの中型有棘細胞は，麻酔下のみならず徐波睡眠状態（いわゆる「深い眠り」の状態）でも状態間ゆらぎを示すことから[2]，状態間ゆらぎは麻酔による副次的な現象ではないことがわかる．しかし，状態間ゆらぎの線条体における機能はほとんどわかっていない．覚醒状態でじっとしているラットの中型有棘細胞では，2つの安定した状態が見られなくなることが報告されている[2]．このことは，ゆらぎが睡眠中の情報

処理にだけ関係していることを意味しているのかもしれない．しかし，上述のように，線条体は運動の制御と密接にかかわっている．したがって，運動中のラットで状態間ゆらぎが起こるか否かを確かめることは重要である．しかし，動いている動物からの細胞内電気記録は現在の技術ではほとんど不可能である．

次に，状態間ゆらぎが起こる仕組みであるが，中型有棘細胞の状態間ゆらぎは大脳皮質からの入力を反映したものに過ぎないと考えられている[3]．その根拠の1つは電極から細胞に電流を流しても状態遷移が誘発されないことである[3]．このことは，細胞膜自体には2つの安定した状態を生じさせる特性がないことを意味している．もう1つの根拠は，大脳皮質からの入力を遮断するとダウン状態からアップ状態への遷移が見られなくなることである[3]．

### 2.2 小脳

ラットとブタの小脳にあるプルキンエ細胞も膜電位の状態間ゆらぎを示す[4]．小脳もやはり運動と深くかかわっており，小脳へ損傷を受けると運動の学習が阻害される他，精密な運動ができなくなったり体のバランスをとるのが難しくなったりする．小脳は脊髄などから運動に関する情報のみならず，感覚情報も受け取っている．そして，小脳での情報処理の結果はプルキンエ細胞の活動を通して他の部位に出力される．

プルキンエ細胞の状態間ゆらぎの研究は麻酔下のみで行われている．ラットの場合状態遷移は自発的に起こっているが，ヒゲに刺激を加えると，細胞がダウン状態にあるときはアップ状態への遷移が，アップ状態にあるときはダウン状態への遷移が誘発される[4]．これらの現象がもし運動中のラットでも起きているのなら，運動に伴う感覚情報の変化がプルキンエ細胞の状態遷移のダイナミクスに反映されることになり興味深い．

線条体の中型有棘細胞と異なり，プルキンエ細胞は非線形力学系の観点から興味深い性質をもっている．膜電位がダウン状態にあるプルキンエ細胞に脱分極する方向の電流を電極から短時間流すと，細胞の膜電位がアップ状態に遷移し，逆に，膜電位がアップ状態にあるプルキンエ細胞に過分極する方向の電流を短時間流すと，膜電位がダウン状態に遷移する[4]．これらのことは，2つの安定した膜電位が，個々の細胞の膜自身がもつ性質に由来することを示唆している．さらに，安定した2つの状態が非線形系でよく見られることを考えると，その性質は膜に発現しているイオンチャネルの開閉確率の非線形な電位依存性である可能性が高い．プルキンエ細胞に関してさらに興味深いのは，ダウン状態にある細胞にさらに過分極する方向の電流を短時間流すとアップ状態への遷移が誘発されることである[4]．また，上記のヒゲへの刺激では，脱分極する方向の電流が同様の現象，つまりアップ状態からダウン状態への遷移を引き起こす．すなわち，同じ方向の刺激（過分極方向の通電やヒゲの刺激による脱分極性応答）が，そのときの細胞の状態に応じて逆向きの遷移（アップ状態への遷移やダウン状態への遷移）を引き起こすのである．

これらの現象を定性的に説明するために1つの細胞モデルが提案された[4]．そのモデルでは膜電位と，遅い時定数をもつ過分極活性化カチオン電流（hyperpolarization-activated cation current，逆転電位 −30 mV）を担うチャネルの閉確率が動的変数にとられる．これらの動的変数を支配する2次元非線形方程式の解を相空間（phase space）で解析すると，アップ状態とダウン状態に対応した2つの安定した固定点（fixed point，系が時間変化しない状態に対応する相空間上の点）があらわれる（**Fig. 2**）．この2つの安定固定点の存在は，膜電位を支配する方程式に含まれるナトリウムチャネルが開く確率のもつ非線形な電位依存性に由来している．そして，上記の現象は相空間の大域的な構造，つまりそれぞれの固定点のもつ吸引域（basin of attrac-

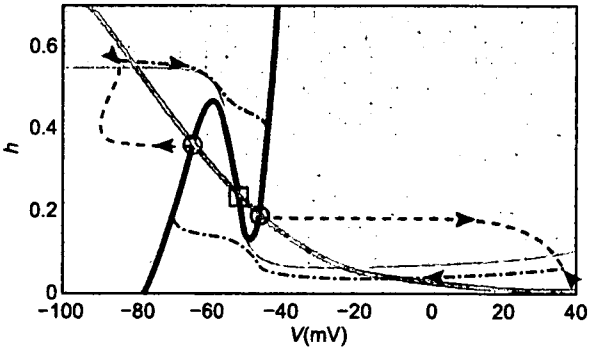


**Fig. 2**
Phase space for the two dynamical variables. The horizontal axis represents membrane potential and the vertical axis inactivation term of the channels for hyperpolarization-activated current. The black and gray solid lines are the nullclines $dV/dt = 0$ and $dh/dt = 0$, respectively. The circles indicate the stable fixed points that correspond to the two stable states of membrane potential, and the square indicates the unstable fixed point. The white line represents the separatrix, which is the border between the basins of attraction of the up (dark gray) and the down state (light gray). Arrows indicate the trajectory of the dynamic variables during (dashed lines) and after (dash-dotted lines) an outward current injection (left) or a simulated stimulus input (right). Adapted from ref. 4 by permission from Macmillan Publishers Ltd: *Nature Neurosci*, copyright (2005).

tion，ある安定固定点の吸引域内にある任意の点を初期条件とすると系は最終的にその固定点に引き込まれる）の拡がり方から説明される（**Fig. 2**）.

### 2.3 大脳皮質

大脳皮質における膜電位の状態間ゆらぎは，ラットやマウスのバレル皮質（ヒゲからの情報を処理する体性感覚野），ネコの第1次視覚野およびその他いくつかの領野で観測されている．ここでは，まずネコの第1次視覚野を例にとって，状態間ゆらぎの機能を考えてみる.

第1次視覚野は大脳皮質において視覚情報を最初に受け取る領野であり，個々の細胞は視覚的に視野に提示された縞模様に応答する．また，応答の強さは縞模様の向きによって異なる（方位選択性）．ちなみにここでいう応答とは刺激提示期間における平均発火頻度の増加のことである．Anderson らは麻酔下のネコにいろいろな向きの縞模様を提示し，アップ状態の平均持続時間と電位が平均発火頻度の方位選択性に対応するような刺激依存性を示すこと，つまり平均発火頻度が高い刺激ほどアップ状態の平均持続時間が長くその電位もより脱分極側にシフトする傾向があることを見いだした[5]．この結果は，刺激に対する平均発火頻度の変化に，状態間ゆらぎの変化が深くかかわっていることを示唆している.

しかし，Haider らはやはり麻酔下にあるネコの第1次視覚野で，Anderson らとは異なり，刺激提示は状態間ゆらぎのダイナミクスに影響を与えないという結果を得た[6]．さらに，アップ状態での電位が刺激に依存した Anderson らの結果とは異なり，Haider らはアップ状態での電位が刺激に依存せず自発的にゆらいでいることを見いだした[6]．また，Haider らは，同一の刺激に対する平均発火頻度で見た細胞の応答は，細胞がアップ状態にあるときのほうが2倍以上大きく，アップ状態での自発的な電位のゆらぎが脱分極するほうへゆらぐほど発火頻度が上昇することを見いだした[6]．これらのことから彼らは刺激に対する細胞応答の利得がアップ状態における脱分極の程度を通して脳の中で内的に調整されており，この利得の調整が情報の選択，特に動物の内的な情報選択に深くかかわっている注意による情報の選択と関係しているのではないかという考えを出している．しかし，覚醒状態のネコで第1次視覚野の状態間ゆらぎを調べた研究はないので，状態間ゆらぎが注意のような動物の内的な状態を反映しているのかどうかは明らかではない．また，なぜ Anderson らと Haider らの結果が異なるのかは今後解決されなければならない問題の1つである.

次に大脳皮質における状態間ゆらぎ発生の仕組みについて見てみる．線条体と異なり，大脳皮質の場合は脳切片でも状態間ゆらぎが観測されること[7)-9)]から，ゆらぎが他の脳部位からの入力に依存せず自律的に起こっている可能性が高い．これを説明するために，先の小脳における仕組みとはまったく独立に，再帰的な興奮性結合を考慮に入れたモデルが提案されている[8)]（ちなみに小脳には再帰的な興奮性結合はない）．すなわち，ネットワークの一部の細胞が自律的に発火する仕組みを内包しており，それらの細胞の発火に誘発されたアップ状態への遷移がネットワークを構成する再帰的な興奮性結合を通してすべての細胞に急速に伝わるというモデルである．このモデルでは近傍の抑制性細胞からの入力によってバランスされた再帰的な興奮性入力を通してアップ状態が維持される．そして，細胞が発火している間に遅い時定数をもったナトリウム依存性カリウムチャネルが活性化してくることで興奮性が抑えられ，ネットワーク全体の興奮性が維持できなくなったときダウン状態への遷移が起こる.

アップ状態の維持とダウン状態への遷移の仕組みが異なるが，アップ状態への遷移に再帰的な興奮性結合が重要な役割を果たしているモデルは他にも提案されている[10)]．フェレット前頭皮質の脳切片に興奮性シナプスの働きを阻害する薬を投与した実験では，一部の細胞のアップ状態への遷移を伴わない自発的な発火を残して，アップ状態への遷移が見られなくなるという結果が得られている[7),8)]．この結果はアップ状態への遷移に興奮性結合が深く関与していることを示唆している．また，上記2つのモデルでは，ネットワーク全体がある程度の周期性をもって，アップ状態とダウン状態を繰り返す．これは，徐波睡眠状態で個々の細胞の状態間ゆらぎが脳波と同期しており，ネットワークレベルでゆらぎにある程度の周期性が見られるという実験結果[11)]とも定性的に一致する.

さて，われわれが感覚情報に基づいて行動を計画したり，推論など論理操作を行うときに，一時的に情報を保持したり操作したりすることが必要になる．このとき使われる記憶のことを作業記憶という．上記のように，再帰的な興奮性結合を通して，ネットワークレベルでアップ状態への遷移と維持が達成される場合，個々の細胞はアップ状態にある間発火し続けることが可能である．そして，この持続的な発火が作業記憶に対応する神経活動ではないかという説が提案されている．しかし，それを裏付ける実験的証拠は見つかっていない.

## 3. サル

はじめにも書いたように，状態間ゆらぎの研究をサルで行うには，細胞内電気記録によって直接状態間ゆらぎを観測するのではなく，細胞外電気記録された発火活動をモデルを使って解釈するというのが唯一の有効な方法である．そして，このような考えにたって行われた研究が2つある．1つは北野らが行ったサルの線条体の中型有棘細胞に関する研究である[12]．彼らは，覚醒状態にあるサルの大脳皮質の運動野に電気刺激を与え，そこから入力を受けている中型有棘細胞が発火するタイミングを計る実験を繰り返した．すると，発火の遅延の分布関数に2つのピークがあらわれた．彼らは，中型有棘細胞の詳細な細胞モデルを使ったシミュレーションで，2つのピークは膜電位に2つの状態があると仮定するとよく説明できることを示した．この研究は，サルにおいて状態間ゆらぎが存在する可能性を初めて示したのみならず，それを覚醒状態にある動物で示したという点で重要である．

さて，「2.1 線条体」の項で記述したように，線条体における状態間ゆらぎは大脳皮質からの入力のゆらぎを反映していると考えられている．したがって，サルの線条体で状態間ゆらぎが見られることは，サルの大脳皮質でも状態間ゆらぎが起こっている可能性を示唆している．それを，北野らとはまったく異なるモデルと発火活動の記録の組み合わせで示したのが著者らの研究である[13]．著者らの研究では麻酔下のサルの下側頭葉視覚連合野（TE野）から複数の細胞の発火活動を同時に記録した（**Fig. 3**）．TE野は，物体像の知覚および認識において重要な働きをしている大脳皮質の領野である．著者らは細胞が自発的に発火している状態で記録を行い，記録された発火系列の自己相関関数，細胞間の相互相関関数などの統計的性質を調べた．そして，それらの性質が，細胞の発火頻度が膜電位の状態間ゆらぎに応じて2状態マルコフ過程（2つの状態をもち，遷移確率が現在の状態にだけ依存する確率過程）にしたがって変化しており，細胞間でその変化が同期しているというモデル（**Fig. 3**）で定量的に説明できることを示した．このことは，TE野の細胞が発火頻度の異なる2つの状態間をゆらいでおり，かつそのゆらぎが細胞間で同期していることを示唆している．著者らの研究はサルの大脳皮質で状態間ゆらぎが起こっている可能性を初めて示した研究である．また，状態間ゆらぎが2状態マルコフ過程で記述されることから，ゆらぎに周期性がないことになり，周期性の見られる脳波との関連は薄い可能性が高い．これは徐波睡眠時に状態間ゆらぎが脳波と相関をもつネコの大脳皮質の細胞などとは異なっており，ゆらぎ発生の仕組みを考える上で興味深い．また，非常に多くの神経細胞の集団的な活動を反映していると考えられる脳波との相関が低いと見られるにもかかわらず，状態間ゆらぎの細胞間同期が見られたことも，状態間ゆらぎ発生の仕組みや機能を考える上で興味深い．

## 4. おわりに

本稿では，膜電位の状態間ゆらぎについてその機能と仕組みを見てきた．状態間ゆらぎはさまざまな動物のさまざまな脳の部位で観測される現象である．しかし，その機能については動物，部位を問わずなお不明な点が多い．そして，そのおもな原因の1つは行動や課題を行っている動物から細胞内電気記録を行えないことである．また，ここまでの記述から明らかなように，状態間ゆらぎの仕組みや機能をより深く理解する

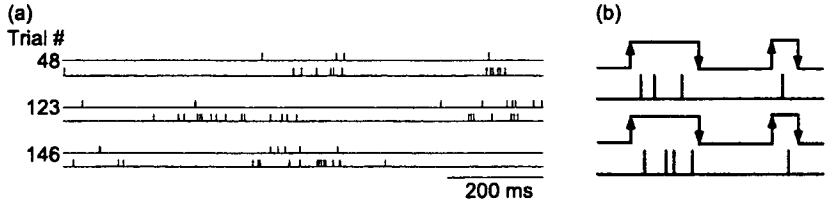


**Fig. 3**
Firing pattern of TE neurons and the Markov model of two states fluctuation. (a) Experimentally recorded spike activities on three trials are shown. For each trial, activity of one neuron is indicated in the top and that of the other in the bottom row. The vertical lines represent spike timing. For each neuron, there are two distinct periods: the period during which the neuron fires (firing period) and the period during which the neuron does not fire (non-firing period). Moreover, firing periods and non-firing periods of the neurons overlap well, respectively. These characteristics are qualitatively consistent with the results of our model analysis. (b) A schematic diagram of our model. For a neuron pair, synchronized two-state Markov processes describe fluctuations in firing rates of the neurons that are likely to correspond to membrane potential fluctuations (the top and the third trace from the top). The neurons fire only at the up-state (the second from the top and the bottom trace).

ためにはネットワークレベルでの細胞活動を研究することが不可欠であると思われるが，細胞内電気記録は同時に多数の細胞から記録を行うことができない．今後細胞内電気記録に関するこれらの問題が克服されるかどうかはわからないが，行動や課題を行っている動物を用いてネットワークレベルでの状態間ゆらぎの研究を行うには，細胞内電気記録以外の方法をとるのが現時点では現実的であるように思われる．その1つとして考えられるのはサルで用いられているような，発火活動の記録とモデルを組み合わせた研究である．近年，行動や課題を行っている動物から多数の電極を用いて同時に多くの細胞の発火活動を記録できるようになってきたので，この方法は有効であると思われる．別の方法として考えられるのは，2光子顕微鏡によるカルシウムイメージングである．マウスの視覚野の脳切片を用いた実験では，細胞内カルシウム濃度の上昇と，細胞のアップ状態とがよく対応するという結果が得られている[9]．また，顕微鏡の小型化により，行動中の動物から多数の細胞の活動を同時にイメージングする技術も開発されてきている[14]．

最後に，モデルの研究からもわかるように状態間ゆらぎに関する研究は，神経科学の分野のみならず，非線形力学系，非平衡統計物理学などの観点からも興味深い．このようなことから状態間ゆらぎの研究は生物物理学の研究テーマとしてふさわしいと思われる．この特集記事によって1人でも多くの方がこのテーマに興味をもっていただければ幸いである．

## 文　献


1) Stern, E. A., Kincaid, A. E. and Wilson, C. J. (1997) *J. Neurophysiol.* **77**, 1697-1715.
2) Mahon, S., Vautrelle, N., Pezard, L., Slaght, S., Deniau, J., Chouvet, G. and Charpier, S. (2006) *J. Neurosci.* **26**, 12587-12595.
3) Wilson, C. J. and Kawaguchi, Y. (1996) *J. Neurosci.* **16**, 2397-2410.
4) Loewenstein, Y., Mahon, S., Chadderton, P., Kitamura, K., Sompolinsky, H., Yarom, Y. and Haeusser, M. (2005) *Nature Neurosci.* **8**, 202-211.
5) Anderson, J., Lampl, I., Reichova, I., Carandini, M. and Ferster, D. (2000) *Nature Neurosci.* **3**, 617-621.
6) Haider, B., Duque, A., Hasenstaub, A. R., Yu, Y. and McCormick, D. A. (2007) *J. Neurophysiol.* **97**, 4186-4202.
7) Sanchez-Vives, M. and MaCormick, D. (2000) *Nature Neurosci.* **3**, 1027-1034.
8) Compte, A., Sanchez-Vives, M., MaCormick, D. and Wang, X. (2003) *J. Neurophysiol.* **89**, 2707-2725.
9) Cossart, R., Aronov, D. and Yuste, R. (2003) *Nature* **423**, 283-288.
10) Kang, S., Kitano, K. and Fukai, T. (2004) *Neural Netw.* **17**, 307-312.
11) Steriade, M., Timofeev, I. and Grenier, F. (2001) *J. Neurophysiol.* **85**, 1969-1985.
12) Kitano, K., Cateau, H., Kaneda, K., Nambu, A., Takada, M. and Fukai, T. (2002) *J. Neurosci.* **22**, RC230(1-6).
13) Uchida, G., Fukuda, M. and Tanifuji, M. (2006) *Phys. Rev. E* **73**, 0319101-0319106.
14) Brecht, M., Fee, M. S., Garaschuk, O., Helmchen, F., Margrie, T. W., Svoboda, K. and Osten, P. (2004) *J. Neurosci.* **24**, 9223-9227.



内田　豪

**内田　豪（うちだ　ごう）**
理化学研究所脳科学総合研究センター研究員
東京工業大学大学院理工学研究科博士後期課程修了（理学博士）後，東京大学先端科学技術研究センターCOE研究員，理化学研究所脳科学総合研究センター研究員，理化学研究所基礎科学特別研究員を経て現職．
研究内容：生命系におけるゆらぎ
連絡先：〒351-0198　和光市広沢2-1
E-mail: guchida@brain.riken.jp

# Preservation of Macular Oscillatory Potentials in Eyes of Patients with Retinitis Pigmentosa and Normal Visual Acuity

*Kazuteru Ikenoya, Mineo Kondo, Chang-Hua Piao, Shu Kachi, Yozo Miyake, and Hiroko Terasaki*

**Purpose.** To study the functional changes in the macula of the retina in the early stage of retinitis pigmentosa (RP), by analyzing each component of the focal macular electroretinogram (fmERG).

**Methods.** fmERGs were recorded from 39 patients with RP with normal visual acuity (>1.0) under direct fundus observation using a modified infrared fundus camera and 5°, 10°, and 15° stimulus spots. The amplitudes and implicit times of the a-wave, b-wave, and oscillatory potentials (OPs) in the patients with RP were compared to those from 30 age-similar normal control subjects.

**Results.** The amplitudes of the different components of the fmERGs in patients with RP ranged from severely reduced to normal. The degree of amplitude reduction increased as the size of the stimulus spot increased in the patients with RP. The relative amplitudes of the OPs (67% of the mean in normal subjects) were better preserved than that of the b-wave (46%) and the a-wave (39%) in a 10° spot in the patients with RP.

**Conclusions.** The relative preservation of the OPs in the patients with RP could be due to either the buffering effect of the large receptive fields of the OP generators or to the retinal remodeling after the progressive loss of photoreceptors. Recordings of each component of fmERG can provide important information on the different layers of the central retina in RP eyes and can add to the understanding of the pathophysiology of RP. (*Invest Ophthalmol Vis Sci.* 2007;48:3312-3317) DOI: 10.1167/iovs.06-1417

Retinitis pigmentosa (RP) is a group of inherited retinal degenerations characterized by progressive loss of photoreceptors and eventual widespread atrophy of the retina.[1-4] The initial visual impairment in patients with RP is usually night blindness and visual field loss in the periphery; the central visual function is usually affected at the later stages of the disease. RP is genetically heterogeneous. At present, approximately 40 genes have been identified as causing RP (http://www.sph.uth.tmc.edu/retnet/ provided in the public domain by the University of Texas Houston Health Science Center, Houston, TX).

From the Department of Ophthalmology, Nagoya University Graduate School of Medicine, Nagoya, Japan.

Supported by Grant-in-Aid 18591913 (MK), and 18390466 (HT) from the Ministry of Education, Science, Sports and Culture, Japan.

Submitted for publication November 29, 2006; revised January 9, 2007; accepted April 9, 2007.

Disclosure: **K. Ikenoya**, None; **M. Kondo**, None; **C.-H. Piao**, None; **S. Kachi**, None; **Y. Miyake**, None; **H. Terasaki**, None

The publication costs of this article were defrayed in part by page charge payment. This article must therefore be marked "*advertisement*" in accordance with 18 U.S.C. §1734 solely to indicate this fact.

Corresponding author: Mineo Kondo, Department of Ophthalmology, Nagoya University Graduate School of Medicine, 65 Tsuruma-cho, Showa-ku, Nagoya 466-8550, Japan; kondomi@med.nagoya-u.ac.jp.

Because the central retinal function is relatively better preserved than the peripheral retina until the late stages of RP, it is important to evaluate the functional changes in the macular area of patients with RP, not only for visual prognosis but also for studying the pathophysiology of the disease processes. The full-field electroretinograms (ERGs) have traditionally been used to assess objectively the retinal function of patients with RP. However, the full-field ERG is a mass potential from the entire retina, and it is not known how the local macular function contributes to the full-field ERG. To overcome these problems, focal (f)ERGs[5-9] and multifocal (mf)ERGs[10-17] have been used to assess the macular function of eyes with RP, because these techniques can elicit electrical activities from localized retinal areas. However at present, there are no results on the alterations of the a-wave, b-wave, and oscillatory potentials (OPs) in the maculae of patients with RP.

Thus, the purpose of this study was to determine the functional changes in the different retinal layers of the macular area by analyzing each component of the focal macular (fm)ERGs at a relatively early stage of RP. We wanted to determine whether the amplitudes of OPs are better preserved than those of the a- and b-waves in the maculae of patients with RP. Our results are the first clinical demonstration that neural activities from the inner retina are better preserved than those from the middle and outer retina in the macular area of patients with RP.

## Methods

### Subjects

We retrospectively reviewed the fmERGs of 127 patients with RP (62 men, 65 women), that were recorded from 1987 to 2006 in the Department of Ophthalmology, Nagoya University Hospital. The clinical diagnosis of RP was based on the funduscopic findings, visual fields, and ISCEV (International Society for Clinical Electrophysiology of Vision) standard full-field ERGs.[18] The inclusion criteria were patients with RP who had received a complete medical examination including best corrected visual acuity, fundus examination, Goldmann kinetic visual field, full-field ERGs, and fmERGs; patients whose best corrected visual acuity was 1.0 or better; patients whose Goldmann kinetic visual fields by the I4e target were of a >5° radius; and those whose amplitude in the fmERG for 15° stimulus spot was detectable (>0.4 μV). We used these inclusion criteria for the definition of early-stage RP, because most patients with RP whose visual acuity is <0.8 or whose Goldmann kinetic visual fields by I4e target were <5° had undetectable fmERGs. Waveform analysis was very difficult or impossible in these patients because of the severely reduced fmERGs.

The exclusion criteria were patients with atypical RP (e.g., central RP, sector RP, or unilateral RP), patients with opacities in the media including cataracts, and patients with cystoid macular edema. If the fmERG were recorded from both eyes with visual acuity of >1.0, the data from the right eye were used for the analyses. The Goldmann kinetic visual fields were determined with the V4e and I4e white test light against the standard white background of 31.5 apostilbs.

Based on the inclusion and exclusion criteria, the fmERGs of 39 eyes of 39 patients with RP (18 men, 21 women; mean age, 37.9 ± 15.4



Investigative Ophthalmology & Visual Science, July 2007, Vol. 48, No. 7